Corrosion characteristics of Al alloy/galvanized-steel Couple in NaCl solution

Pin Du[1], Jianzhong Li[1,2,*], Yanliang Zhao[2], Yigang Dai[2], Zhongdong Yang[1], Yanwen Tian[1]

[1] School of Metallurgy, Northeastern University, Shenyang city, 110819, China
[2] State Key Laboratory of Development and Application Technology of Automotive Steels (Baosteel Group), Shanghai Baoshan 201900,China
[*]E-mail: lijz@smm.neu.edu.cn

The corrosion characteristics of EN 6061-T6/ hot-galvanized IF steel jointed with tox punching and self-piercing rivets was compared using electrochemical impedance spectra, SEM, XPS, and EDS in sodium chloride solution. The results demonstrate that EN 6061-T6/hot-galvanized IF steel subject to tox punching presented more severe galvanic corrosion than the self-piercing rivet joint. The potential difference in the connected position can be promoted by the formation of a closed circuit corrosion current, leading to severe corrosion. Punching joint strained condition, such as extrusion and stretching, can potentially affect the corrosion performance of the partial region. The EIS of the stressed area showed obvious difference contrast to steel/aluminum sheets, especially the stretched region. The pitting corrosion of EN 6061-T6 appeared due to its electrochemical performance and the similarity between the potential difference in heterogeneity and pitting potential.

1. INTRODUCTION

The rapidly developing transportation system and commonly used mechanical transmission engineering, and their combination in the automotive industry require product in both manufacturing and performance. Improvements include resource savings, fast implementation for assembly, and durability. To lower energy consumption the automotive industry has introduced light metals to replace fractional traditional steel. In particular, high tensile aluminum alloys have become a popular focus for lightweight design concepts [1,2]. To achieve the assembly and performance requirements, the connection placements of different materials need to be broadly considered.

Currently, several methods are employed to install rivet joints, including tox punching and self-piercing rivets (SPR), which are form-fitting link connections with wide applicability. To evaluate the advantages and disadvantages of jointing properties among various materials with diverse elemental components and geometrical dimensions, this study focuses on galvanized-steel/Al alloy.

Transition temperatures of pure phase are distinct in phase diagrams, and the formation of certain intermetallic compounds in the wield joints have a negative influence on the strength of connecting position, e.g., tensile strength. Mechanically-placed rivet joints can mitigate risks brought by intermetallic compounds [3], i.e., $FeAl_2$, Fe_2Al_5, $FeAl_3$. Meantime they also meet the demands of high speed automated procedure. Furthermore, using composite constructions can increase the breaking strength to more than sexfold that of wield joints [4,5]. Joints between a variety of metallic texture specimens should be compared to evaluate their electrochemical behavior. Finally, investigating corrosion and metal utilization has implications in efficiently using global metal resources [6–10].

Several pertinent studies [11–15] have investigated the corrosion properties of rivet joints, they found that chlorine ions expedite the corrosion process of the connecting materials, particularly Al alloys and carbon steel, which reduces their protective characteristics. L. Krüger [4] investigated the galvanic corrosive properties of SPR joints with two types of aluminum alloy sheets, EN AW-6014-T4 and EN AW-6082-T5, which were connected with blind rivets made of material electrogalvanized carbon steel. The results indicated that the blind rivet with zinc-coated steel had a more negative corrosion potential than the aluminum alloy. The steel substrate has a role as a cathodic protector when the rivet links with the sheets. In another work, M. Mandel [8] studied EN AW-6060-T6 aluminum alloy's pitting sensitivity concatenated with carbon-fiber reinforced plastic (CFRP)/aluminum rivet joints. In the study, the galvanic corrosion evaluation included immersion tests, and finite element simulation. While results were generally in agreement with previous studies, the author also noted that the geometry of the joint can play an important role in the extent of galvanic corrosion. Similar experimental procedures were employed by S. Palani [16], Eva Håkansson [17], and Shengxi Li [18,19], who estimated the corrosion behavior of blind rivet jointed Al with CFRP and carbon steel exposed in a severe outdoor environment. They found that Al coupled with carbon steel undergoes slight corrosion on the outside surface using blind rivets. Furthermore, the corrosion mechanisms include galvanic, pitting, and crevice corrosion after long period exposure in the region with Cl^- [20]. In comparison, steel results in serious corrosion with damage centers in deep crevices [21–23]. Significantly, when the deposition rate of Cl^- increased over a critical value, the corrosive rate increased.

However, these described research studies were short of EIS characterization on the corrosion behavior of joints between Al alloy and carbon steel, and few studies have reported on the corrosion behavior of aluminum connected with steel. The influence of strained condition on corrosion characterization and galvanic corrosion behavior of tox punching and self-piercing rivet joints combining hot galvanized IF steel and the aluminum EN 6061-T6 sheets need to be investigated using an immersion test and EIS in 3.5 wt% NaCl solution. XPS, X-ray Diffraction, Energy Dispersive X-ray, and scanning electron microscopy were applied to identify sample status after corrosion due to exposure to 3.5 wt% NaCl solution.
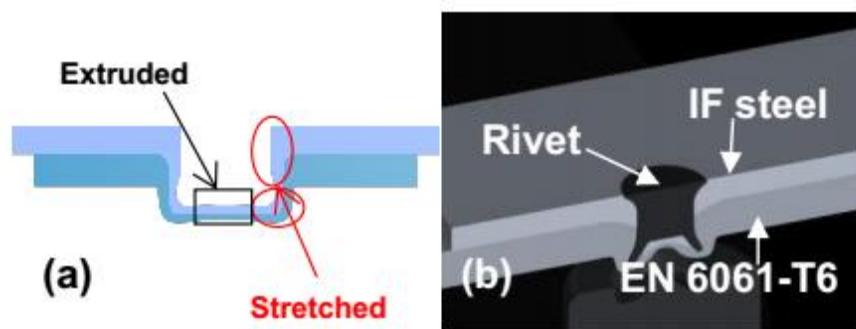
2. EXPERIMENTAL

2.1. Materials preparation

Materials consisted of EN 6061-T6 with 1.5 mm thickness and interstitial free steel (IF steel gauges 0.7 mm thickness) that was hot-galvanized (99.8% Zn and < 0.2% Al) to 5 μm thickness, self-piecing rivets, i.e., Henrob rivet with type C and Φ = 5mm, and rivets select hot-galvanized mild steel with the chemical compositions shown in Table 1. The assembly SPR specimens and tox punching samples were prepared respectively with a hand-hydraulic SPR gun + AUTO Feeder + Controller and TOX® Building Blocks with robotic-/machine-mount tongs. SPR samples were processed at a rivet speed of 250 mm/s with a peak force of 9.5 kN to obtain an appropriate intensity of roots to assure sufficient residual intensity. The maximum press force used in the tox punching was 45 kN with a punch head size of 4.6 mm.

Table 1. Chemical compositions (wt%) of raw materials

Material	C	Si	Mn	P	S	Nb	Ti	B	Mg	Fe
IF steel	0.0016	<0.03	0.14	0.008	0.0066	<0.010	0.067	0.0001	-	Bal.
Rivet	0.33	0.59	0.78	-	-	-	-	-	-	Bal.
Material	Mg	Si	Mn	Cu	Fe	Zn	V	Cr	Ti	Al
6061-T6 Al alloy	0.49	0.53	0.13	0.23	0.70	0.06	0.09	0.09	0.10	Bal.
Rivet surface	-	-	-	-	0.96	Bal.	-	-	-	-

Structural illustrations of the joints cross-section for the two joints are presented in Fig. 1.

Figure 1. The cross-section of samples (a) tox punching and (b) SPR joint

Experimental specimens containing cross-section samples had dimensions of approximately 15 mm × 15mm × 2.2 mm. They were subsequently sanded with 400, 800, and 1200 SiC abrasive paper to remove the heat affected zone caused by the wire-electrode cutting. Ultrasonic cleaning in ethanol and water cleaning with a banister brush was used to remove oil contamination on the working surface of all size marking samples. Finally, the samples were weighed and marked for testing.

2.2. Electrochemical experiments

Potentiodynamic polarization curve, open circuit potential, and EIS of experimental materials were conducted in 3.5 wt% NaCl solution using a three-electrode system and PARSTST® 2273 Advanced Electrochemical System at room temperature. The saturated calomel was used as the reference electrode and the graphite was used as counter electrode. EN 6061-T6, IF steel, and blind rivets were used as the work electrodes in the three-electrode system. To achieve a stable state and precise estimates, the specimens were immersed for 30 min in solution [24]. Subsequently, the EIS tests indicated an amplitude of 0.01 V. The range of the polarization potential was –1.5 V/SCE to 0.5 V/SCE with a scan rate of 0.001 V/s. The tested area of samples was 1 cm^2 for all samples.

In this work, certain equivalent circuits models were tested, which could potentially match the data from the EIS experiment.

2.3. Microstructural characterization

To investigate the trend and mechanism of galvanic corrosion on the aluminum/IF steel rivet joints, 3.5 wt% NaCl solution was used to simulate a marine corrosive environment, i.e., representing automobile sheets in a coastal city with a humid environment. All specimens were immersed in 3.5 wt% NaCl solution at 23 ± 2° temperature for 120 h to reach the critical deposition value. Then, specimens were cleaned with water and a banister brush followed by ultrasonic cleaning in ethanol. The corrosive microstructures of the surface and cross-section, cleaned and uncleaned, were evaluated with an ULTRA PLUS (ZEISS) field emission scanning electron microscope equipped with energy dispersive spectroscopy. Products of all experimental samples were scraped off for analysis by X-ray photoelectron spectroscopy, X-Ray diffraction and Energy Dispersive X-ray. The specimens not subject to corrosion were also analyzed by XPS.

3. RESULTS AND DISCUSSION

3.2. Corrosive characteristics of electrochemical tests

Potentiodynamic polarization curves for the tox punching specimens subject to 3.5 wt% NaCl solution are shown in Fig. 2. This figure and Table 2 show the corrosive characteristics of samples. The current densities between the different structural materials in the anode and cathode region were asymmetrical. The corrosion potential of individual stretched part of the hot-galvanized IF steel was –1.361 V/SCE, and the $E_{corr.}$ of extruded hot-galvanized IF steel was slightly different at –1.351 V/SCE. In comparison, the $E_{corr.}$ of the hot-galvanized IF steel substrate was –1.067 V/SCE. This phenomenon can be attributed to the strained condition of the tested region. In particular, the stretched zone emerged incomplete of Zn coating and lattice imperfections of the surface film showed dislocations from deformation. All of these characteristics would have a significant influence on the electrochemical activity. In comparison, the EN 6061-T6 polarization curves indicated that the

corrosion potential of the stretched zone ($E_{corr.}$ = –0.911 V/SCE) was more negative than the aluminum 6061-T6 sheets ($E_{corr.}$ = –0.821 V/SCE), with the appearance of the depolarizer in the electrolyte.
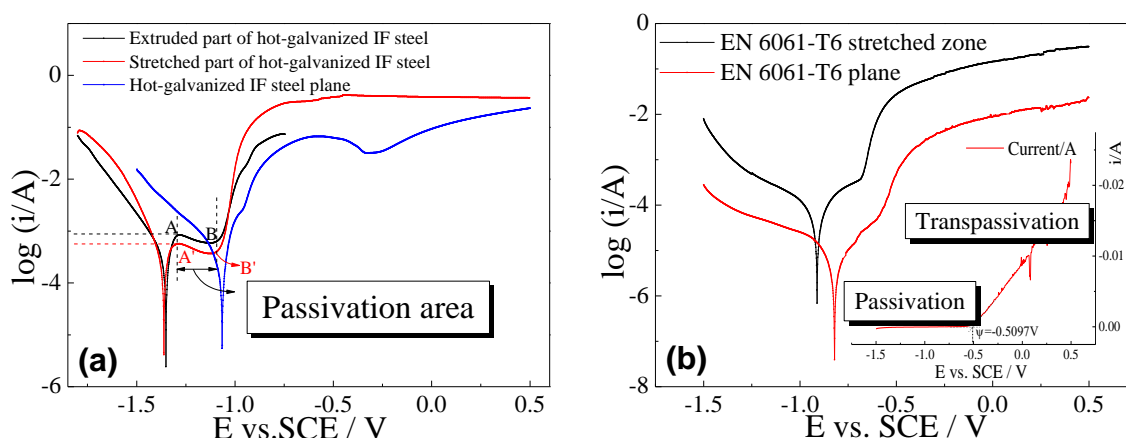
Figure 2. The potentiodynamic polarization curves of tox punching specimens (a) hot-galvanized IF steel and (b) EN 6061-T6

The difference in potential between the stretched hot-galvanized IF steel and EN 6061-T6 sheets was ΔE = 0.54 V. All these results revealed that the hot-galvanized IF steel, and particularly the stretched section, was more activated than EN 6061-T6 in the 3.5 wt% NaCl solution. The stretched hot-galvanized IF steel acted as an anode for preferentially corrosion. This observation was also supported in a later immersion test. The section with connecting materials on the sheets acted as a cathode, which caused the anode reaction to accelerate in the galvanic systems of the tox punching head. The process was in agreement with the contact corrosion effect (γ) between the connected materials, as in Eq. (1) [4,23,25].

$$\gamma = I_{ano1}/I_{corr1} = 1 + A_{cant2}/A_{ano1} \tag{1}$$

$$I_a = (E_{R,c} - E_{R,a})/r_K * A_{cant2}/A_{ano1} \tag{2}$$

where, I_a is the current density of contact corrosion effect and A_{ano1} represents the area of anode in the galvanic field. The symbol r_K is the cathode polarization resistance, which is provided by the joined sheets in this experiment. The higher ratio between the two poles' areas can achieve stronger contact corrosion effects and higher I_a in the galvanic system with the presence of a depolarizer. Furthermore, the aluminum alloy sheets showed severe pitting and crevice corrosion behavior derived from the Cl⁻.

Table 2. The corrosion potential and current density of tox punching specimens

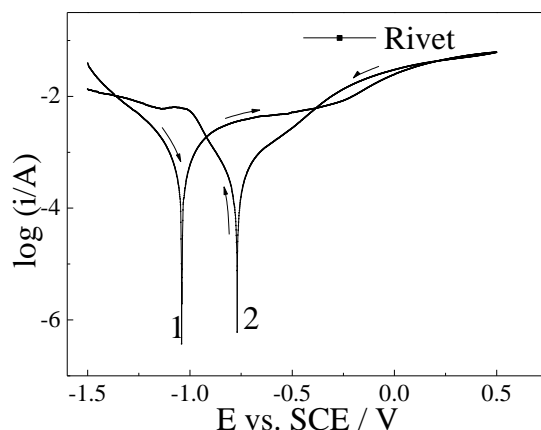| Counterpart	$i_{corr.}$(mA cm⁻²)	$E_{corr.}$(V)	Pitting potential(V)	R_p(Ω cm²)
Extruded part of hot-galvanized IF steel	0.404	–1.351	-	68.2
Stretched part of hot-galvanized IF steel	0.510	–1.361	-	73.7
Individual tested hot-galvanized IF steel sheets	0.267	–1.067	-	97.2
EN 6061-T6 stretched	1.542×10⁻³	–0.911	–0.628	593.7
EN 6061-T6 sheets	1.470×10⁻³	–0.821	–0.510	6371.4

The current density of stretched hot-galvanized IF steel showed a slight increase up to $E = -1.308$ V/SCE and $I = 2.320$ mA/cm^2. Then, a decrease in current density was observed, as shown in Fig. 2a, down to $E = -1.123$ V/SCE and $I = 0.397$ mA/cm^2. Later, the current density gradually increased with a further forward change in potential. The active zone and transpassivation field in the anode polarization curves indicate that the current density of dissolution for hot-galvanized IF steel obeys a semilogarithm rule. All of these observed phenomena stemmed from incomplete dissolution of the Zn coating and an increasing destruction of the passive film with the adsorption and penetration of Cl$^-$. While the reason for a slowing down of current density augment (Fig. 2a illustrated by AB, A'B') was a period of passivation caused by the accumulation of corrosion products and hydrolysis, metal ion adsorption did occur. Referring to the polarization resistance, the stretched positions of two different materials lacked a flow resistivity compared to sheets in the corrosion potential. Different locations of IF steel showed distinct changing trends in the anode polarization curve because of the strained condition, completeness of the surface film, and station of the external crystal structure. Therefore, strained condition, such as extrusion and stretching, should be taken into consideration because of their effect to electrochemical activity.

The potential differences (Fig. 2b) between pitting potential and corrosion potential for the two structural EN 6061-T6 aluminum sheets were respectively $\Delta E_{stretched} = 0.283$ V and $\Delta E_{plane} = 0.313$ V. The appearance of more critical pitting corrosion of the aluminum sheets occur with a closer potential difference in heterogeneity to pitting potential [19,26,27]. Accordingly, the stretched EN 6061-T6 would be more likely to generate corrosion pits.

Comparably, electrochemical information for the SPR rivet is shown in Fig. 3. Table 3 summarizes the corresponding information of the tested materials. As mentioned previously, the two-stage potentiodynamic polarization curves for hot-galvanized IF steel sheets and rivet show asymmetry. The unequilibrium potential has a relationship with the oxygen concentration in the solution. Distinct anode polarization curves between the anoxic zone and oxygen-rich area result from the reaction progress of the anode area, which can be observed later in the process. Hysteresis loops appeared in the graphs for potential (E/V) –log(i/A), except the curves for the EN 6061-T6 sheets (not shown), which was caused by the inhomogeneity of the micro-area composition brought from the anode galvanic change on the metal surface. The characteristics of the plots for the EN 6061-T6 sheets were due to the products and consumption of passive film $Al_2O_3 \cdot H_2O$, Al_2O_3, which caused the reactions in partial areas to intensify and partially weaken. Specifically, the adsorption of Cl$^-$ on the EN 6061-T6 sheets surface would cause an autocatalysis reaction of the partial anode area, which would result in a brief and sharp rising trend in the current.

In comparison, the corrosion potential of hot-galvanized IF steel and rivet was measured as $E_{corr.} = -1.048$ V/SCE. The EN 6061-T6 potential was measured as $E_{corr.} = -0.737$ V/SCE. The rivet in the joint of the rivet-aluminum alloy-hot galvanized IF steel acted as the anode and the EN 6061-T6 sheets acted as the cathode in the 3.5 wt% NaCl solution with the appearance of a depolarizer. However, the rivet-IF steel, particularly the seam, also acted as an anode in the joint of the rivet-hot galvanized IF steel-aluminum alloy. This joint is commonly used to meet the mechanical requirement that rigid materials are punched into mild materials to enable effective and sufficient interlocking with deformation space. From test observations, in the SPR joint, the corrosion of the rivet surface was

slightly faster than the hot-galvanized IF steel, particularly the seam of the SPR and steel had a large number of bubbles.

Figure 3. The potentiodynamic polarization curves of rivet

**Table 3.** The corrosion potential and current density of rivet joint samples

Counterpart	$i_{corr.}$ (mA cm^{-2})	$E_{corr.}$ (V)	R_p (Ω cm^2)	$i_{sec\text{-}corr.}$ (A cm^{-2})	$E_{sec\text{-}corr.}$ (V)	R_p (Ω cm$^{2)}$)
Hot-galvanized IF steel sheets	0.718	−1.054	53.4	4.329×10^{-4}	−0.828	92.4
Rivet	0.627	−1.042	62.7	2.851×10^{-4}	−0.768	122.4
EN 6061-T6 sheets	1.274×10^{-2}	−0.737	3196.6	1.703×10^{-5}	−0.404	2598.6

Graphs of current density for rivet showed gradually increased related to the anode reaction of the Zn coating. These were followed by hysteresis loops before achieving the second increasing corrosion potential. $E_{sec\text{-}corr.} = -0.768$ V/SCE indicates complete dissolution of the Zn coating and a dissolution of substrate materials, which shows that the potential connected with the corrosion potential of carbon steel. More negative values were also shown at higher scan speeds, platforms appeared at a potential of $E_{rivet} = -1.035$ V/SCE with a current density of $i_{rivet} = 5.959$ mA/cm^2. The second corrosion potential shows that the rivet no longer had an anode role and the IF steel sheets is inferior to the rivet and EN 6061-T6 sheets. The measurements indicate that this geometric joint constitution has better corrosive resistance than the tox punching of IF steel and EN 6061-T6 sheet joints due to the small-scaled area ratio (see Eq. (1–2)).

Respectively, Fig.4a, b, c, d, e, Eq. (3) show the Nyquist plots for the tox punching and SPR specimens in 3.5 wt% NaCl solution. The EIS parameters are compiled in Table 4. The Nyquist plots for hot galvanized IF steel and rivet (see Fig. 4a, b, c,) show obvious differences in the corrosion resistance of these materials in 3.5 wt% NaCl solution. These differences correspond to the potentiodynamic polarization curves. Furthermore, the speeds of the two electrode reactions were controlled by the discharge progress of the traversing charged particles, the duration of mass transfer was short, so the concentration polarization can be ignored [28–30].

$$Z_\omega = R_1 + \frac{Z_{Q_1}R_{CT} + Z_{Q_1}Z_f}{R_{CT} + Z_{Q_1} + Z_f} \; ; \; Z_f = \frac{Z_{Q_2}R_3}{R_3 + Z_{Q_2}} \; \text{or} \; Z_f = \frac{j\omega C R_3}{j\omega C + R_3} \; ; \; Z_Q = \frac{1}{(j\omega)^n Q} \; (3)$$

where Q is the CPE-constant, n is the power value (0 < n <1).
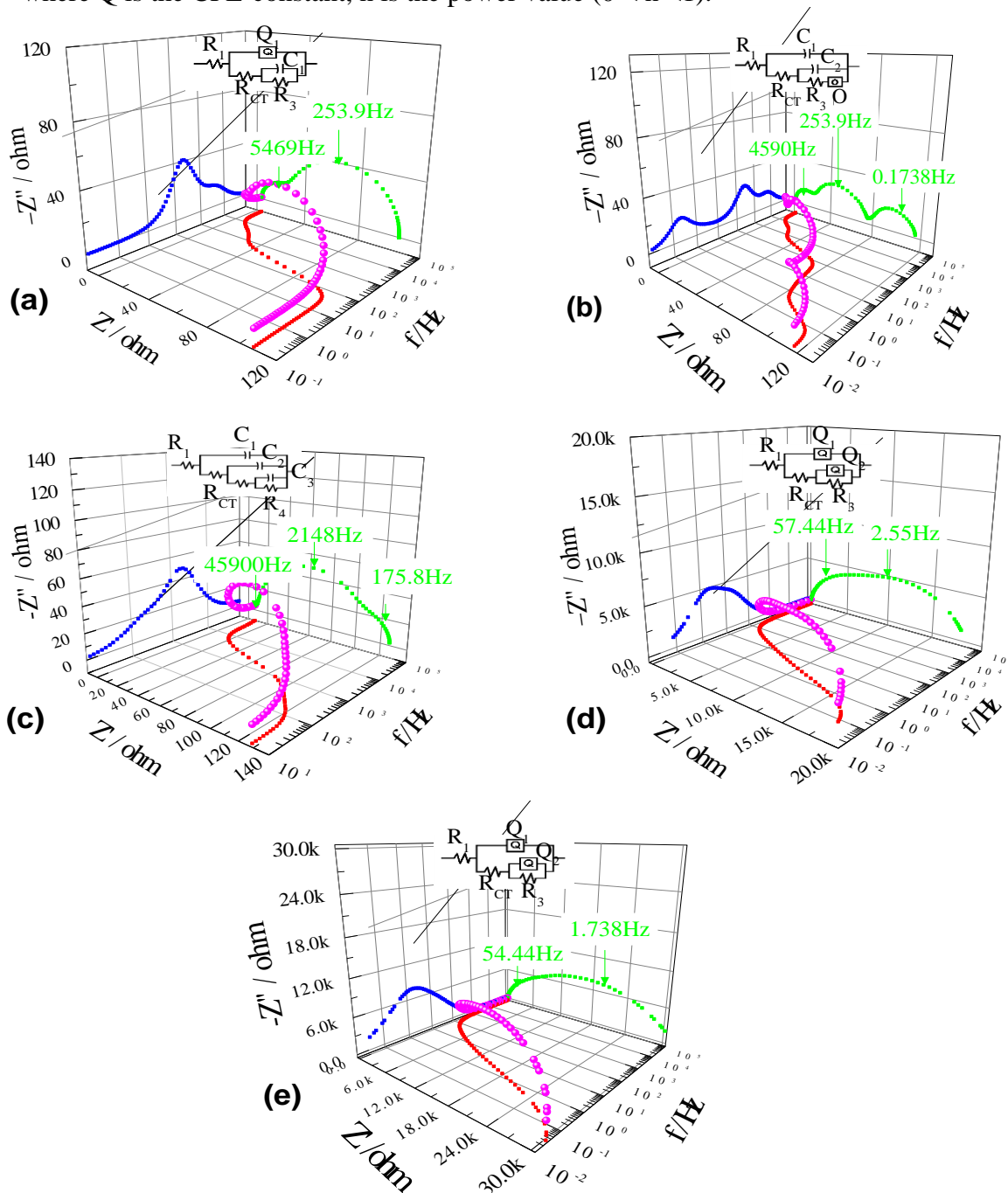
Figure 4. The Nyquist plots of IF steel and rivet specimens in 3.5 wt% NaCl solution (a) IF steel (b) stretched steel (c) SPR rivet (d) stretched EN 6061-T6 (e) EN 6061-T6

The plots for the tested electrode materials show depressed semicircles. These regions appeared as two arcs from high frequencies to lower frequencies, excluding the stretched region for hot-galvanized IF steel and the SPR rivet. This observation indicates that the existence of two time-constants (2 time constants τ_{TC}, τ_w) summarized from Bode, -Phase-log(Freq/Hz) (not shown) reflects the reaction process of these four working electrodes. The first time-constant connecting the high frequencies is derived from the charge-discharge relaxation process for every electrode potential *E*. This is the final result from the combination of resistance from the solution and electrical double-layer

capacitor. The second time-constant, for the lower frequencies, corresponds to the electrical double-layer capacitor from the Zn coating or oxide film ($Al_2O_3 \cdot H_2O$, Al_2O_3) changes derived from the polarization and linear polarization resistance of the Zn coating, oxide film, or corrosion production during metal corrosion. Characteristic frequencies for each stage are calculated in Fig. 4. Larger characteristic frequencies corresponding to a shorter relaxation process relating to Eq. (4, 5):

$$\tau_{TC} = 1/\omega_{max} = R_{CT}C_1 \qquad\qquad (4)$$
$$\tau_w = 1/\omega_{wmax} \qquad\qquad (5)$$

Where ω_{wmax} represents the frequency value that the second arc appears a maximum on the $-Z_i$ (imaginary axis) [26].

The Nyquist spectra of the stretched part of the IF steel and rivet presented three arcs in solution, which indicates that a third state could be influencing the electrode process.

Table 4. The similar parameters of EIS about specimens

| Counterpart	$R_1(\Omega\ cm^2)$	$C_1\&Q$ (F cm^{-2})	$R_2(\Omega\ cm^2)$	$C_2\&Q$ (F cm^{-2})	$R_3(\Omega\ cm^2)$	C_3(F cm^{-2})	$O\&R_4(\Omega\ cm^2)$
Stretched IF steel	1.587	1.171×10^{-6}	27.32	1.385×10^{-5}	44.83	3.497×10^{-2}	1.47
IF steel sheets	8.627	4.969×10^{-5}	141.30	1.796×10^{-2}	132.80	–	–
Rivet	4.715	2.335×10^{-7}	10.02	6.436×10^{-7}	92.93	4.307×10^{-7}	19.34
EN 6061-T6 stretched	21.200	1.685×10^{-6}	7214	1.679×10^{-5}	9803	–	–
EN 6061-T6 sheets	16.640	9.369×0^{-7}	8624	1.147×10^{-5}	24820	–	–

As shown in figures, the resistance spectra for the experimental materials are partially ohmic and capacitive in 3.5 wt% NaCl solution. The AC response values increased as the frequencies declined. The former response of arc is the proof of uniform dissolution and breakup of the $Al_2O_3 \cdot H_2O$, Al_2O_3, or Zn coating. Their diameters with two time constants were correspondingly equal to R_2, the transfer resistance for the charging progress in the double electrode layer. The plane region for the IF steel and EN 6061-T6 have larger resistances than the deformed zone (particularly the stretched region) which indicates a more powerful resistance in the corroding environment. The following resistance arc is related to the incomplete dissolution of surface materials adjacent to the grain boundaries [31]. Derived from the breakup and stretch cracks of the Zn coating, the stretched IF steel had the lowest resistance value. The last arc information is in agreement with the characteristics of the adhered voluminous corrosion products, and similar to the interface of the porous electrode. O represents the impedance of finite diffusion layer on the surface of stretched IF steel samples. As shown in Table 4, the values of C_2 and C_3 at lower frequencies are higher than C_1 at higher frequencies, especially the C_3 for the IF steel stretched region, which reached 0.03497 F cm^{-2}.

After deformation, the R_p value of the samples decreased, which indicates that their corrosion resistance weakened in 3.5 wt% NaCl solution. This behavior was due to areas with Zn coating and oxide film decreasing, incomplete and imperfect lattices of the surface film, emerging dislocations, and helical dislocation stair endpoints, which were arose from plastic deformation, e.g., extrusion and

stretch, that providing more active area for atoms to leave the lattice to the metal surface for adsorption on the planar plane in the electrolyte solution.

The work electrode and particle transfer mechanism are presented in Fig. 5. For the complete electrode process, the phase boundary reactions maintain the balance. Hydrated cations might emerge in the diffuse layer of the double electrode layer so that the honeycomb texture can influence the conductivity of the interface layer (see Fig. 5a).

The electrode roles for the anode and cathode are shown in Fig. 5b. The cathode reaction (see Eq. (6, 7)) depends on the concentration of the depolarizer O_2 in the 3.5 wt% NaCl [32]:

$$O_2 + 2H_2O + 4e^- \rightarrow 4OH^- \quad (6)$$
$$2H_2O + 2e^- \rightarrow 2OH^- + H_2 \quad (7)$$
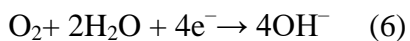
The anode reaction occurs first, as Eq. (8), then Zn^{2+} ions combine with OH^- (see Eq(1–2)) to generate the precipitation adsorbed on the surface of the electrode (Eq. (9)).

$$Zn \rightarrow Zn^{2+} + 2e^- \quad (8)$$
$$Zn^{2+} + 2OH^- \rightarrow Zn(OH)_2 \quad (9)$$
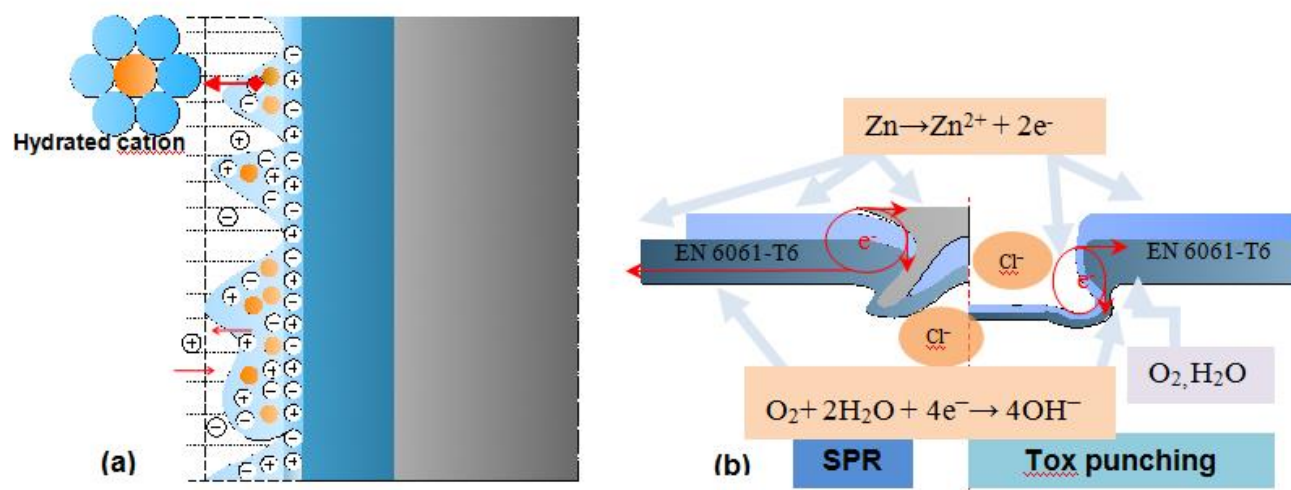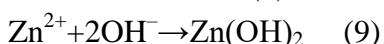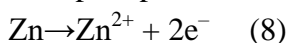
Figure 5. The structural illustration of interface layer (a) from left to right: solution; double electrode layer (diffuse layer & close bed); cladding material/oxide film; base metal and (b) electrolyte reaction.

Accordingly, closed-circuit circulation was created and the corrosion process sostenuto proceeded. Related to the potentiodynamic polarization curves (see Fig. 2, 3), voluminous corrosion behaviors occur with conspicuous cracks and severe intergranular corrosion along grain boundaries. The optical micrograph (not shown) of the initial status of EN 6061-T6 before the electrochemical experiments shows Mg_2Si precipitation separated out as the main second-phase particle with large-sized particles mounted into the grain interiors and small-sized precipitation distributed along the crystal boundaries [33]. The corrosion potential of Mg_2Si in 3.5 wt% NaCl solution was measured Kruehong [26] as $E_{corr.} = -1.21$ V/SCE, which is more negative than the voltage of EN 6061-T6. Therefore, the high-activity Mg_2Si precipitation initially dissolved and flowed, causing serious dealloying of intermetallic compounds when Cl^- ions penetrated the oxide film. Subsequently, the Al alloy substrate will gradually start to dissolve. The serious reaction are shown as Eq. (10, 11):

$$Mg_2Si+2H_2O \rightarrow 2Mg^{2+}+SiO_2+4H^++8e^- \quad (10)$$
$$Al \rightarrow Al^{3+}+3e^- \quad (11)$$
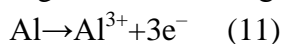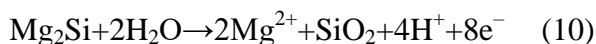
This phenomenon could not be evaluated using galvanic corrosion progress, but instead was evaluated via the self-corrosion of EN 6061-T6 material with the emerging Cl^- [4,24].

3.2. Characterization of immersion test

The SEM micrographs (not shown) of the EN 6061-T6 before immersion corrosion in 3.5 wt% NaCl show a discrete interface area and mild scratches. Fasciculate zona and flow lines from the stretched region are observed. These would have great influence on the electrochemical activity of the zone as compared to the original sheets. The XPS results (see Fig. 6a) show that the surface compositions are mainly Al_2O_3 and $Al(OH)_3$. The SEM graph (not shown) of a riveted hot-galvanized IF steel joint before corrosion, showing a porous structure on the specimen surfaces. However, the SPR rivet interface is incomplete. Zn was the primary material observed on the surface of the hot-galvanized IF steel (see Fig. 6b).
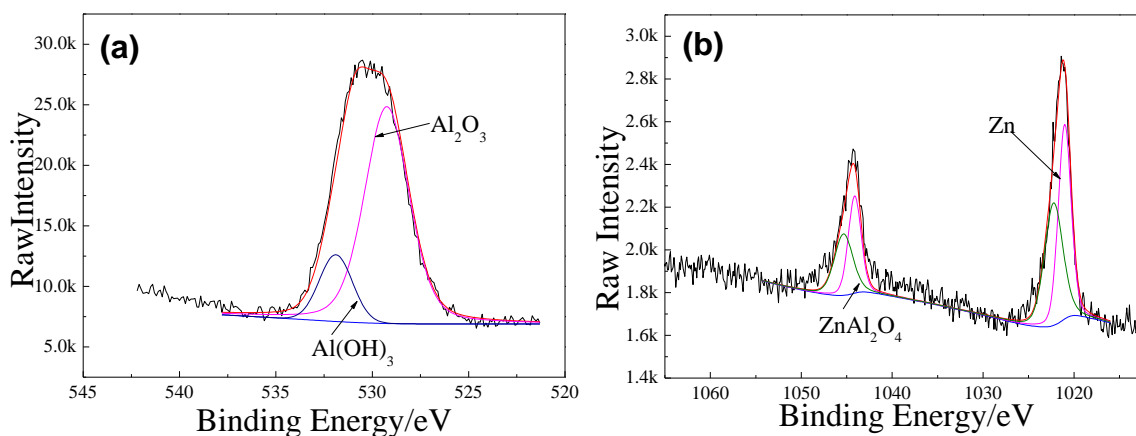
Figure 6. Representative XPS spectra (a) EN 6061-T6 (b) hot-galvanized IF steel

Fig. 7 show corrosion interface micrograph and EDS for rivets jointed with hot galvanized IF steel after the immersion test in 3.5 wt% NaCl solution. As shown, the assembled samples with SPR joints formed uniform corrosion, which is in contrast to rivet joints described by V. Fiore [34].

The NaCl attack sites in the Zn coating of the hot-galvanized IF steel resulted in subsidence holes, indicating activated areas that adsorbed negative ions, especially the region of incomplete coating. The mechanically installed SPR rivet had corrosion similar to that of Zn coated IF steel. Attribute to the phenomenon which real exposed area was bigger than the apparent area, power lines can not restrain themselves uniformly.
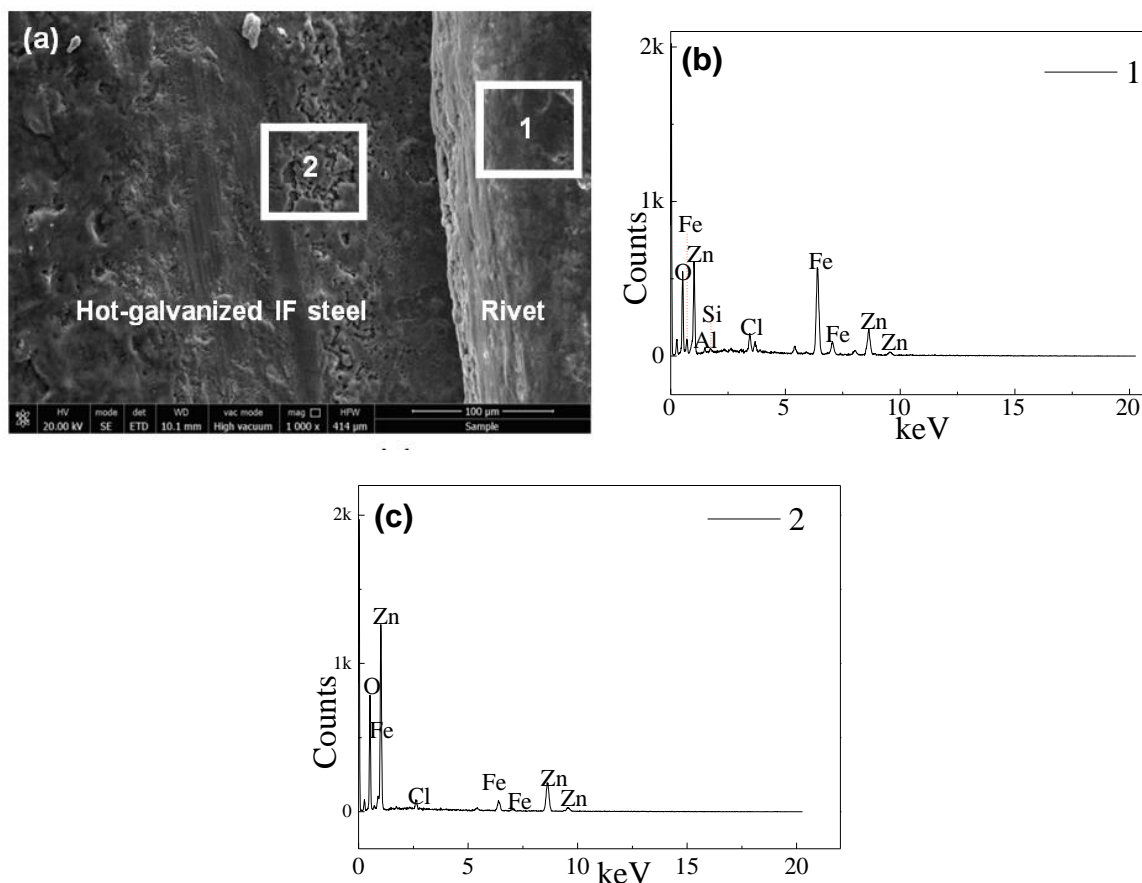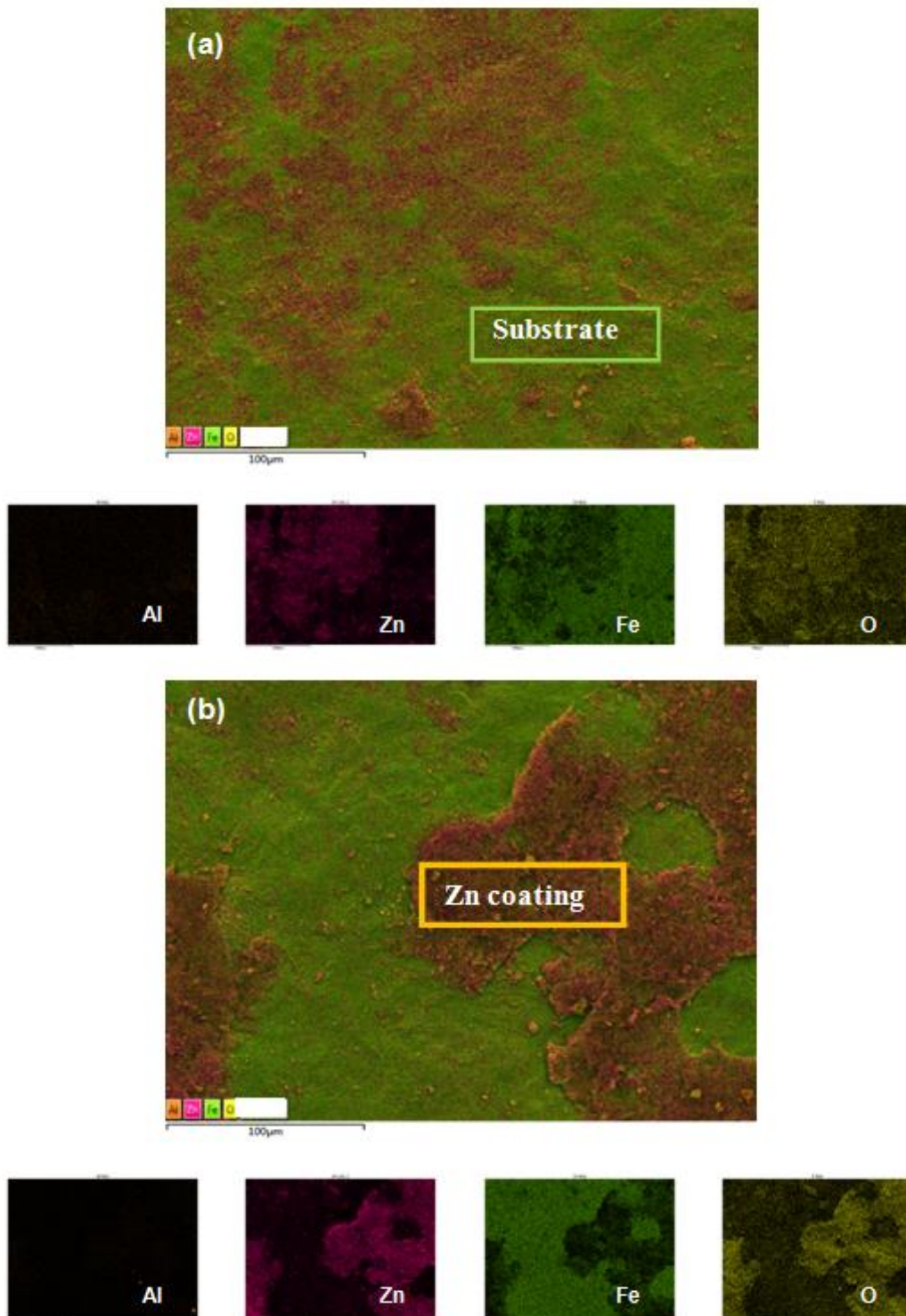
Figure 7. (a) SEM micrograph (b) EDS of rivet and (c) EDS of hot galvanized IF steel after corrosion

The status (see Fig. 8) for different strained condition combined with the electrochemical data, prove the presence of activities distinction between differing strained condition. Fig. 8a shows that the stretched zone corroded after a period and the Zn coating of the exposed area was uniformly destroyed. A comparison of the observed loading systems are shown in Fig. 8b (the extruded zone). The image shows that the Zn coating partially disappeared, and Fe appeared uniformly in the region absent of Zn coating. The EDS spectra for deformed EN 6061-T6 had the same characteristics (not shown), the oxide film of the extruded region partially disappeared. These results prove that the loading methods have a significant influence on the corrosion behavior of hot galvanized IF steel.

Fig. 9a, b show the partial acerose corrosion products adhered and apparent cracks dispersed on the surface of EN 6061-T6. The observed film exfoliation and pitting holes are in agreement with prior observations [35]. The region scratched with an external force clearly corroded. After the disappearance of the surface film, second-phase particles Mg_2Si fell off preferentially to the extent that the holes deepened and the concentration differences of the depolarizer and the concentration differences of chloride ions in the microcell made the corrosion complicated. From Fig. 9c partial scallops and embossment resulted from Si and Al in the alloy matrix. Apparently, the presence of Si in the ratio can be attributed to the corrosion products producing SiO_2 from the immersion solution. Part region contained Zn, which may be carried by electrode reaction process and particle transferring.

According to all the results presented, tox punching units were subject to fierce galvanic corrosion affected by closed-circuit circulation. Strained condition showed significant influence on the

pitting corrosion of Al alloy and steel. SPR assembled specimens suffered uniform corrosion due to the small-scale area ratio between cathode and anode.

Figure 8. EDS of hot galvanized IF steel after corrosion (a) stretched and (b) extruded region
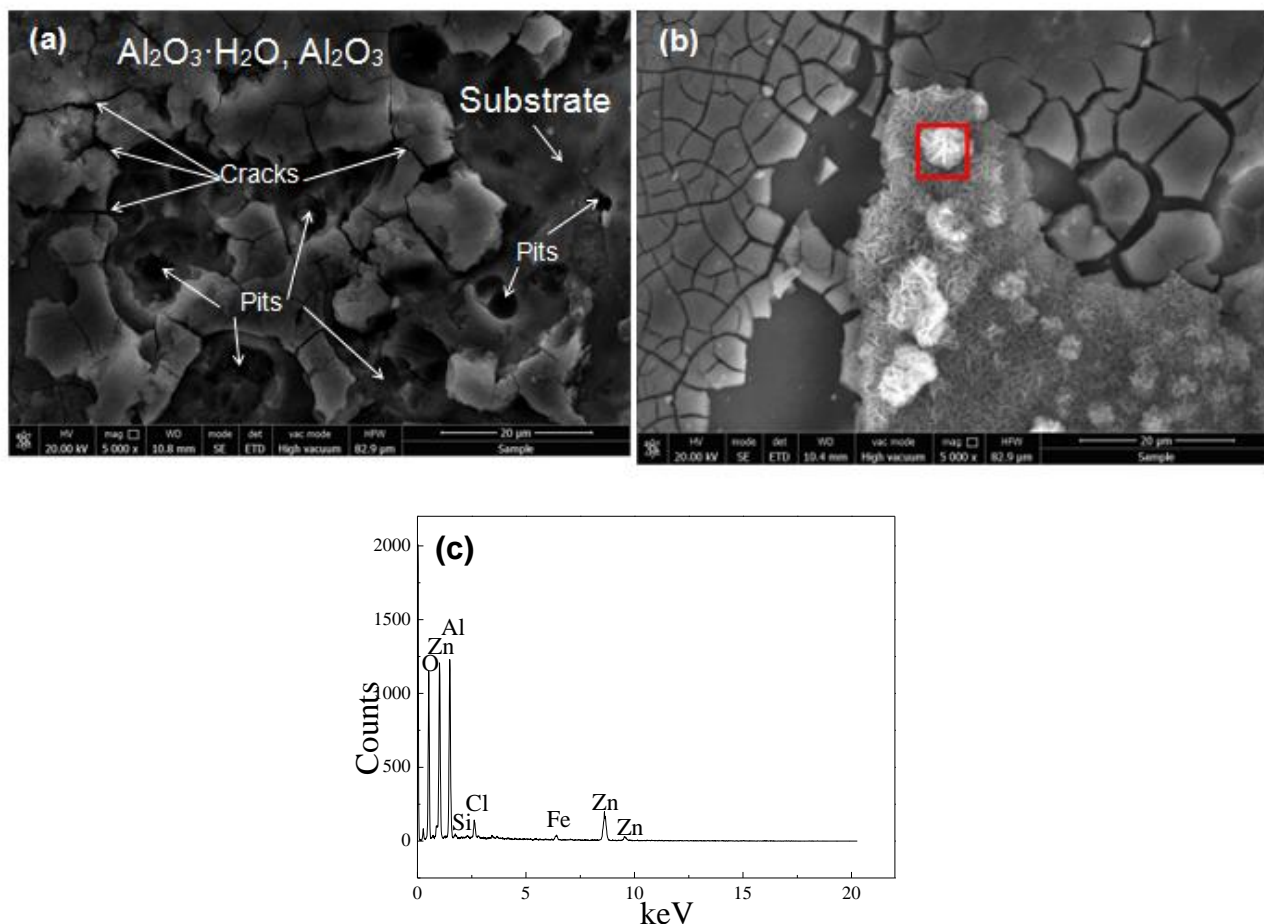
Figure 9. (a), (b) SEM micrograph and (c) EDS of EN 6061-T6 coupled with rivet after immersion

4. CONCLUSION

The experimental results in this study showed the corrosion resistance of different types of samples, which had clear distinguishing characteristics. The corrosion of EN 6061-T6 connected with hot-galvanized IF steel via the tox punching method had galvanic corrosion that was more severe than that of the SPR joints. This contrast was due to the difference in potential ($\Delta E = 0.54$ V) between the stretched hot-galvanized IF steel and EN 6061-T6 sheets. In addition, an intense contact corrosion effect was induced between a large cathode coupling a small stretched Zn coating anode. The EIS of the stressed area showed obvious distinction contrast to IF steel/aluminum sheets, especially the stretched region. Strained condition produced during the tox punching assembly, such as extrusion and stretching, should be taken into consideration because of their potential effect on electrochemical and corrosion performance in the presence of a depolarizer in an aggressive environment.

The pitting corrosion of EN 6061-T6aluminum alloy specimens was partial due to a pitting potential that was different from the potential difference from heterogeneity. Nonetheless, high density deep etch pits and cracks were found in the SEM micrograph. The stretched region of EN 6061-T6 showed particularly zona fasciculate and flow lines brought from deformation. These can generate film

exfoliation, pitting holes, the adherence of partial acerose corrosion products, and dispersed microscopical cracks. Corrosion is more easily observed in the mechanically stretched region in the aluminum sheets, which is attributed to both the facilitation of pitting and galvanic action by deformation.

References

1. W. F. Xu, J. H. Liu, *Corros. Sci.,* 51 (2009) 2743.
2. L. Q. Guo, X. M. Zhao, B. C. Wang, Corros. Sci., 70 (2013) 188.
3. J. Wloka, H. Laukant, U. Glatzel, S. Virtanen, Corros. Sci., 49 (2007) 4243.
4. L. Krüger, M. Mandel, *Corros. Sci.,* 53 (2011) 624.
5. R. Gravina, N. Pébère, A. Laurino, C. Blanc, *Corros. Sci.,* 119 (2017) 79.
6. M. Jariyaboon, A. J. Davenport, R. Ambat, B. J. Connolly, S. W. Williams, D. A. Price, *Corros. Sci.,* 49 (2007) 877.
7. B. Zaid, D. Saidi, A. Benzaid, S. Hadji, *Corros. Sci.,* 50 (2008) 1841.
8. M. Mandel, L. Krüger, *Corros. Sci.,* 73 (2013) 172.
9. D. Prabhu, P. Rao, *Arabian J. Chem.,* 10 (2017) S2234.
10. I. Jureviciute, S. Bruckenstein, A. R. Hillman, *Electrochim. Acta,* 51 (2006) 2351.
11. M. Mouanga, P. Berçot, J. Y. Rauch, *Corros. Sci.,* 52 (2010) 3984.
12. G. Hölzl, G. Luckeneder, H. Duchaczek, *Corros. Sci.,* 127 (2017) 222.
13. D. Persson, D. Thierry, O. Karlsson, *Corros. Sci.,* 126 (2017) 152.
14. S. Li, H. Khan, L. H. Hihara, J. Li, *Corros. Sci.,* 111 (2016) 793.
15. K. B. Deshpande, *Corros. Sci.,* 62 (2012) 184.
16. S. Palani, T. Hack, J. Deconinck, H. Lohner, *Corros. Sci.,* 78 (2014) 89.
17. E. Håkansson, J. Hoffman, P. Predecki, M. Kumosa, *Corros. Sci.,* 114 (2017) 10.
18. S. X. Li, H. Ali Khan, L. H. Hihara, H. Cong, *Corros. Sci.,* 132 (2018) 300.
19. S. X. Li, L. H. Hihara, *J. Electrochem. Soc.,* 162 (2015) C495.
20. L. Guan, B. Zhang, J. Q. Wang, *Corros. Sci.,* 80 (2014) 1.
21. M. Morcillo, B. Chico, J. Alcántara, I. Díaz, *J. Electrochem. Soc.,* 163 (2016) C426.
22. E. D. Kiosidou, A. Karantonis, G. N. Sakalis, *Corros. Sci.,* 137 (2018) 127.
23. I. Adlakha, B. Gholami Bazehhour, N. C. Muthegowda, *Corros. Sci.,* 133 (2018) 300.
24. R. K. Gupta, N. L. Sukiman, M. K. Cavanaugh, B. R. W. Hinton, *Electrochim. Acta,* 66 (2012) 245.
25. G. A. Zhang, L. Y. Xu, Y. F. Cheng, *Electrochim. Acta,* 53 (2008) 8245.
26. C. Kruehong, G. A. EL-Mahdy, A. Nishikata, T. Tsuru, *Corros. Sci.,* 52 (2010) 2379.
27. K. A. Yasakau, M. L. Zheludkevich, S. V. Lamaka, M. G. S. Ferreira, *Electrochim. Acta,* 52 (2007) 7651.
28. W. Liu, Q. Li, M. C. Li, *Corros. Sci.,* 121 (2017) 72.
29. J. L. Huang, J. F. Li, D. Y. Liu, *Corros. Sci.,* 139 (2018) 215.
30. M. J. RodrõÂguez Presa, H. L. Bandey, R. I. Tucceri, M. I. Florit, D. Posadas, A. R. Hillman, *Electrochim. Acta,* 44 (1999) 2073.
31. K. M. Behbahani, P. Najafisayar, M. Pakshir, M. Shahsavari, *Corros. Sci.,* 138 (2018) 28.

32. M. Jönsson, D. Persson, D. Thierry, *Corros. Sci.,* 49 (2007) 1540.
33. A. Perovic, D. D. Perovic, G. C. Weatherly, D. J. Lloyd, *Scripta Mater.,* 41 (1999) 703.
34. V. Fiore, L. Calabrese, E. Proverbio, *Composites Part B,* 108 (2017) 65.
35. K. L. Moore, J. M. Sykes, P. S. Grant, *Corros. Sci.,* 50 (2008) 3233.